# Self-energy corrected DFT-NEGF for conductance in molecular junctions: An accurate and efficient implementation for TRANSIESTA package applied to Au electrodes

Joel G. Fallaque[1,3,†], Sandra Rodríguez-González[2], Fernando Martín[1,3,4] and Cristina Díaz[5,‡]

[1] Instituto Madrileño de Estudios Avanzados en Nanociencia (IMDEA-Nanociencia), Cantoblanco 28049 Madrid, Spain

[2] Departamento de Química Física Módulo 14, Universidad Autónoma de Madrid, 28049 Madrid, Spain

[3] Departamento de Química Módulo 13, Universidad Autónoma de Madrid, 28049 Madrid, Spain

[4] Condensed Matter Physics Center (IFIMAC), Universidad Autónoma de Madrid, 28049 Madrid, Spain

[5] Departamento de Química Física, Facultad de Ciencias, Universidad Complutense de Madrid, 28040, Madrid, Spain

E-mail: joel.fallaque@imdea.org[†] and crdiaz08@ucm.es[‡]

30 July 2022

**Abstract.** In view of the development and the importance that the studies of conductance through molecular junctions is acquiring, robust, reliable and easy-to-use theoretical tools are the most required. Here, we present an efficient implementation of the self-energy correction to density functional theory (DFT) non-equilibrium Green functions (NEGF) method for TRANSIESTA package. We have assessed the validity of our implementation using as benchmark systems a family of acene complexes with increasing number of aromatic rings and several anchoring groups. Our theoretical results show an excellent agreement with experimentally available measurements assuring the robustness and accuracy of our implementation.

Submitted to: *J. Phys.: Condens. Matter*

## 1. Introduction

The possibility of using single molecules as active components of electronic devices go back to the 70's, when Aviran and Ratner [1] reported that a single molecule can show rectifier properties. Since then, the number of studies devoted to this topic has continuously increased [2, 3, 4]. From the experimental point of view, several methods have been proposed to construct and analyze molecular junctions. Break junctions techniques (see [5] and Refs. therein) and noise spectroscopy (see [6] and Refs. therein)

are the most popular techniques but other methods have been also proposed [7, 8, 9]. However, due to the intrinsic complexity of these experiments, theoretical modeling is often required to rationalize the experimental results. Due to the large number of atoms needed to model the geometry and the electronic properties of these electrode-molecule-electrode systems, density functional theory (DFT) seems the most efficient simulation method. However, it is well known that mean-field level DFT cannot properly describe the properly electronic interactions beyond linear conductance [10, 11, 12, 13]. But, in combination with non-equilibrium Green functions (NEGF), DFT has been shown to yield transport properties in reasonable agreement with experimental measurements (see [10, 11, 12, 13] and Refs. therein).

In applying the DFT-NEGF method, a self-consistent field calculation is first performed within the Kohn-Sham formalism in the so-called scattering region, which comprises the molecule and some electrode layers. Subsequently, within the Landauer formalism [14], transmissions and conductances are calculated by means of Green's functions. In this procedure, there is a shortcoming to overcome to get results in quantitative agreement with experiment (e.g., at the same level as the accurate, but expensive, GW method based on many-body perturbation theory [15, 16, 17, 18, 19]): the underestimation of the HOMO-LUMO gap, which is the result of the self-energy interaction error in the exchange-correlation (XC) functional and the lack of description of image charge effects [20, 21, 22]. To overcome these shortcomings associated to the standard DFT-NEGF method, several options have been proposed, and developed. A scheme that has received attention during the last few years is based on the use of range-separated hybrid (RSH) functionals[23, 24]. Optimally tuned RSH functionals have been shown to provide, for example, good frontier orbital energies for physisorbed and chemisorbed molecule-surface interface systems[25] and to yield conductance values comparable to the experimental ones [26]. However, RSH functionals are not yet implemented in the most popular periodic boundary conditions (PBC) based codes used to study molecular junctions, which has spurred the development of an alternative scheme in which the HOMO-LUMO energy gap obtained from a local or semi-local functional based-calculation is corrected, the so-called DFT+$\Sigma$ method [27, 28, 29, 30, 31]. This method has revealed as an excellent approach for those systems where the electrode-molecule coupling is weak[17].

In a very simple model, Quek et al. [27] computed the transmission functions using a DFT-based scattering-state approach within the Landauer formalism as implemented in SCARLET [32] and, subsequently, the transmissions was first improved using a net self-energy correction, computed by shifting the theoretical value of the gas phase HOMO to match the experimental ionization potential (IP), which increases the HOMO-LUMO gap, and shifting the HOMO according to the image-charge correction, which reduces the gap. This latter correction was computed by using a simple image-charge model in which a single electron charge is placed in the middle of the molecule. The net self-energy correction of the LUMO level was calculated to be equal and opposite to that of the HOMO. A similar approach was used by Mowbray et al. [28] to study the

influence of the functional groups on charge transport in molecular junctions, although these authors shifted the vacuum HOMO to the -IP computed at DFT level, and the image charge effect was included by removing an electron and approximating the charge distribution associated with the HOMO and LUMO orbitals by Mulliken charges.

Few years later, Quek et al. published an improved version of their formalism [29, 30] in which the self-energy correction is added explicitly to the scattering-state Hamiltonian. In this revised implementation, the self-energy correction of the HOMO (LUMO) level is performed by shifting the theoretical value of the gas phase HOMO to match the experimental ionization potential (electron affinity, EA) and the image potential energies were obtained by placing an image plane at 1 Å from the metal surface; the charge distributions associated with the HOMO and LUMO orbitals were approximated by Mulliken charges. A similar procedure was implemented in the GPAW code [33] by Markussen et al. [17], although, in this case, the image-charge effect was calculated classically as an infinite mirror interaction using a point-charge distribution function. All these procedures mentioned above rely on periodic boundary conditions (PBC) calculations. A different approach has been adopted by Zotti et al. [31], who have used a cluster model to implement, in the TURBOMOLE DFT package [34], a procedure similar to Ref. [29], but employing Mulliken populations for a given orbital (HOMO or LUMO) in the image-charge correction. Going back to PBC-based calculations, very recently, Montes et al. [35, 36] have implemented the self-energy correction in SIESTA/TranSIESTA[13] adding explicitly the correction into the system Hamiltonian using an orbital dependent operator. In their methodology, the image charge effect is corrected by including an electrostatic interaction between a molecular wavefunction charge centered in an atom with its two image charges, one above the top image plane and one below the bottom image plane.

In the present work, we have implemented the DFT+$\Sigma$ correction in TranSIESTA including a shift of the frontier orbitals and the image charge effect. As in the above mentioned methods, the first effect is taken into account by shifting the HOMO (LUMO) level of the free molecule in gas phase to its IP (EA) computed at DFT level. The second effect is included following the approach presented by Markussen et al. [17], but correcting a term used by these authors. The approach we have adopted to account for the image charge in our DFT+$\Sigma$ implementation for TranSIESTA is the main difference with the method proposed by Montes et al. [35]. Unlike in Ref. [35], in our implementation we account for the classical Coulomb interaction between the charge distribution of the HOMO/LUMO orbital of the molecule and *all* the image charges (not just its own reflections) generated by the electrode screening, considering an infinite number of reflections (not just one) of the molecular charge by the two metallic electrodes.

In summary, our model is similar to that of Ref. [17] but applied to TranSIESTA instead of GPAW. It differs from the model presented in Ref. [31] in the scheme of the image charges and the use of PBC instead of the cluster model; and it differs from the model presented in Ref. [35] in the use of infinite reflections to describe the interaction

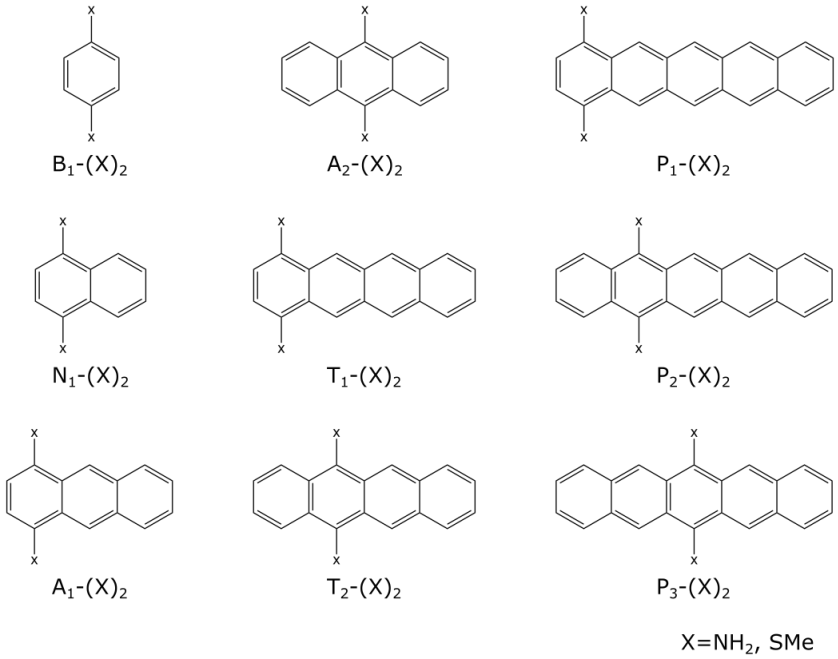


Figure 1: Nomenclature of the molecules studied. Where X represents the anchoring group.

of a charge with the corresponding images charges. Using this new implementation, we report conductance values for several acenes molecules (from 1 to 5 coupled rings) anchored to gold electrodes by means of methyl sulfide (SMe) and amine ($NH_2$) linkers in cis position (see Fig. 1). We have assessed the robustness and accuracy of our implementation by changing several characteristics of the system such as aromaticity, type of anchoring group, and anchoring position. We show that our methodology yields excellent quantitative agreement with experimental measurements, even better than that obtained with previous theoretical implementations.

## 2. Theoretical methods

### *2.1. Theoretical background*

Generally speaking, to compute the conductance (G) of a molecule anchored to two electrodes, we rely on the Landauer formulation [14] and the DFT-NEGF method, so that the transmission function in the momentum space ($k$-space), $T_k$, is obtained from the retarded ($\boldsymbol{G_k}$) and advanced ($\boldsymbol{G_k^\dagger}$) Green's functions. Thus, if we consider a molecule anchored to a left (LE) and right (RE) semi-infinite electrodes (see Fig. 2), the corresponding $T_k$, due to the applied potential $V$, is computed using a self-consistent field Kohn-Sham formalism carried out in the scattering region, SR, (see Fig.2). Within this formalism, $T_k$ is computed as:

$$T_k = \mathrm{Tr}[\boldsymbol{G_k}\boldsymbol{\Gamma_{L,k}}\boldsymbol{G_k^\dagger}\boldsymbol{\Gamma_{R,k}}], \tag{1}$$

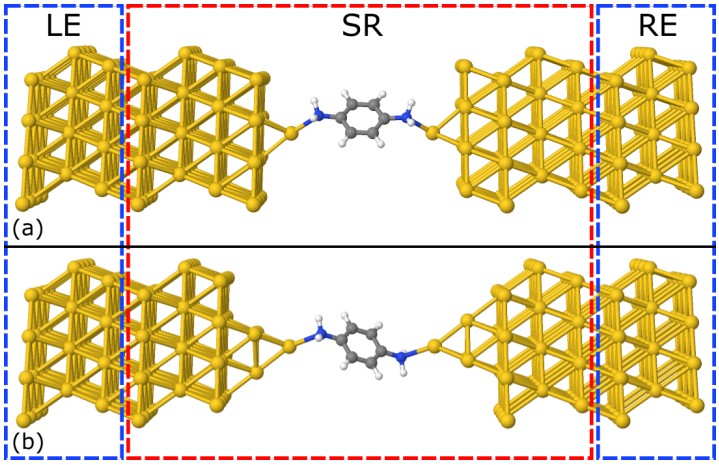


Figure 2: Scheme of the system. Left (LE) and right (RE) semi-infinite electrodes are represented by the blue dashed boxes, and the scattering region (SR) by the red dashed box. (a) Perpendicular molecule with gold surface in adatom configuration. (b) Tilted molecule with gold surface in tip configuration.

where

$$\boldsymbol{G_k}(\varepsilon) = [(\varepsilon + i\eta)\boldsymbol{S_k} - \boldsymbol{H_{KS,k}} - \boldsymbol{\Sigma_{L,k}}(\varepsilon) - \boldsymbol{\Sigma_{R,k}}(\varepsilon)]^{-1} \tag{2}$$

and

$$\boldsymbol{\Gamma_{L/R,k}}(\varepsilon) = i[\boldsymbol{\Sigma_{L/R,k}}(\varepsilon) - \boldsymbol{\Sigma^{\dagger}_{L/R,k}}(\varepsilon)] \tag{3}$$

In these equations, $\boldsymbol{\Sigma_{L/R,k}}$ represents the self-energy of the left/right electrode and $\boldsymbol{\Gamma_{L/R,k}}$ is the associated broadening matrix at $k$ in the scattering region. $\boldsymbol{H_{KS,k}}$ and $\boldsymbol{S_k}$ are the one-particle Kohn-Sham hamiltonian and overlap matrices in the orbital basis at $k$, respectively. Finally, $\boldsymbol{G_k}$ is evaluated at the energy $\varepsilon$ with a small positive constant $\eta = 0^+$ (see Ref. [13]). The results obtained within this formalism can be improved using the many-body GW method, replacing the xc potential, $\boldsymbol{V_{xc,k}}$, by the GW self-energy, $\boldsymbol{\Sigma_{GW,k}}(\varepsilon)$, as following:

$$\boldsymbol{G_{GW,k}}(\varepsilon) = [(\varepsilon + i\eta)\boldsymbol{S_k} - (\boldsymbol{H_{KS,k}} - \boldsymbol{V_{xc,k}}) - \boldsymbol{\Sigma_{L,k}}(\varepsilon) - \boldsymbol{\Sigma_{R,k}}(\varepsilon) - \boldsymbol{\Sigma_{GW,k}}(\varepsilon)]^{-1}. \tag{4}$$

In this equation, $\boldsymbol{V_{xc,k}}$ has been subtracted from the DFT hamiltonian, $\boldsymbol{H_{KS,k}}$, and the GW self-energy $\boldsymbol{\Sigma_{GW,k}}(\varepsilon)$ has been added. However, the GW self-energy depends on $\boldsymbol{G_k}(\varepsilon)$, and therefore, both, $\boldsymbol{\Sigma_{GW,k}}(\varepsilon)$ and eq. 4 have to be solved self-consistently. This method is computationally very expensive and is only affordable for small systems [17, 37, 38]. A reasonable low-cost alternative to obtain conductance values in good agreement with experiment is the so-called DFT+$\Sigma$ approach [29]. In this work, we present an implementation of this approach in TranSIESTA package [13].

### *2.2. DFT+Σ approach*

Aiming to improve the DFT-NEGF method in terms of the conductance, we have evaluated and implemented the non-self-consistent self-energy corrected DFT+Σ approach [29] to the TranSIESTA package [13]. This method is divided in two steps: (i) the correction of the frontier orbitals energy levels as for a free molecule in gas phase; (ii) the inclusion of image charge effects by Coulomb interactions.

*2.2.1. Frontier-orbital corrections* As shown by Janak et al [39], one can estimate the HOMO (LUMO) energy,based on the Koopmans' theorem[40], as the negative of IP (EA). Therefore, the energy shift to correct the HOMO (and all occupied states) and LUMO (and all unoccupied states) energies, is equal to $(-\varepsilon_H - IP)$ and $(-\varepsilon_L - EA)$, respectively. To perform this correction in our case, we have used the same molecular geometries as in the junction. The IP and EA are calculated as:

$$IP = E(+e) - E(0) \tag{5}$$

$$EA = E(0) - E(-e) \tag{6}$$

$E(0)$ being the total energy of the neutral molecule, $E(+e)$ the total energy of the positively charged molecule, and $E(-e)$ the total energy of the molecule with an extra electron. These energies, as well as $\varepsilon_{H/L}$, were computed with the licensed code Gaussian16[41], using the DFT-PBE[42] method in combination with the 6-31G(d) basis set. Notice that the used of Gaussian16 is not a requirement of our approach. Same energies can be obtained from any other quantum chemistry code provided that the same functional and basis set are used.

*2.2.2. Image-charge correction* We have also taken into account image charge effects due to the electrode screening. When a molecule approaches a metallic surface the point charge distribution of its orbitals generates image charges of opposite sign. To put this effect into play, we have to considered the image planes outside the last layer of the metal, which according to Windawsky et al. [43], are located 1.47 Å below a perfect flat gold surface. A point charge of an orbital $\alpha$, $q_i^\alpha$, centered in an atom $i$ located between two image planes generates infinite image charges due to the electrodes screening (left and right). In Fig. 3, we display a schematic representation of the position of those image charges with respect to the image planes. As discussed in Ref. [44], the Coulomb interaction of these charges levels up in energy the occupied orbitals and down shift that of the unoccupied ones.

To perform this correction, we have followed the strategy proposed in Refs. [28, 17]. First, we extract the molecular Hamiltonian sub-matrix, $\boldsymbol{H_{mol}}$, from the SR Hamiltonian, $\boldsymbol{H_{KS,k}}$, and from it, we obtain the point charge distribution as:

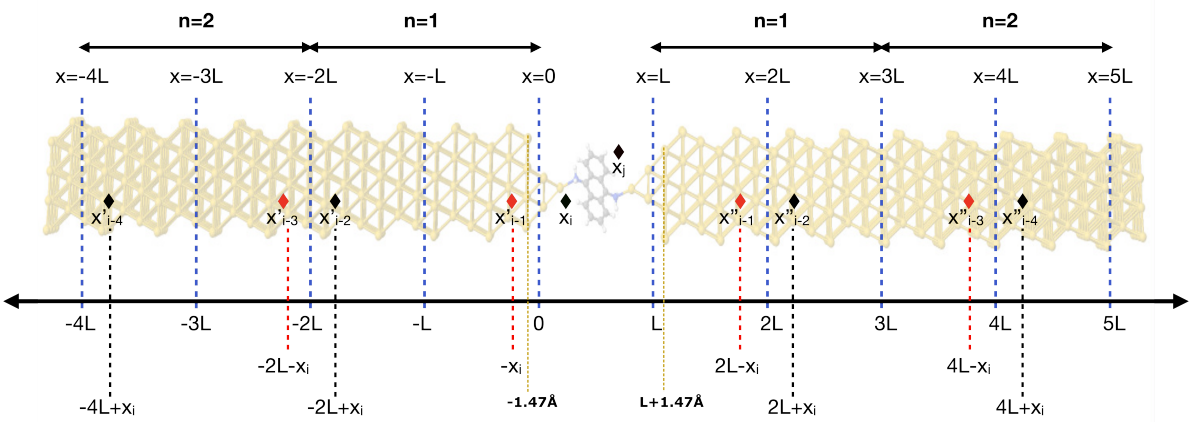


Figure 3: Scheme of the image charges formation by the HOMO/LUMO charge distribution screened by right and left electrodes. Red and black rhombus define the opposite charge sign. $x = 0$ and $x = L$ represent the position of the image planes at 1.47Å outside the surface layer average, in watermark.

$$\rho_\alpha(r) = -e \sum_i \sum_\nu |c^\alpha_{i,\nu}|^2 \delta(r - R_i) \tag{7}$$

$R_i$ representing the coordinates of the atom, and $c^\alpha_{i,\nu}$ the coefficient associated with the orthonormal orbital $\boldsymbol{\phi_{i,\nu}}$ of atom $i$ in the Linear Combination of Atomic Orbitals (LCAO) expansion, $\boldsymbol{\varphi^\alpha} = \sum_i \sum_\nu c^\alpha_{i,\nu} \boldsymbol{\phi_{i,\nu}}$. Then, the point charge of a molecular orbital $\alpha$ centered in an atom $i$, $q^\alpha_i$, is computed as:

$$q^\alpha_i = -e \sum_\nu |c^\alpha_{i,\nu}|^2. \tag{8}$$

From Fig. 3, the image charge correction, $\Delta_\alpha$, due to Coulomb interactions of the $\alpha$ charge distribution is given by:

$$\Delta_\alpha = \frac{1}{8\pi\varepsilon_0} \sum_i \sum_j q^\alpha_i q^\alpha_j \sum_{n=1}^{\infty} \Big( \frac{1}{\sqrt{(x_j + x_i + 2(n-1)L)^2 + r^2_{//,i,j}}} + \frac{1}{\sqrt{(x_j + x_i - 2nL)^2 + r^2_{//,i,j}}} - \frac{1}{\sqrt{(x_j - x_i + 2nL)^2 + r^2_{//,i,j}}} - \frac{1}{\sqrt{(x_j - x_i - 2nL)^2 + r^2_{//,i,j}}} \Big) \tag{9}$$

where $\varepsilon_0$ is the permittivity of vacuum and $r^2_{//,i,j} = (y_j - y_i)^2 + (z_j - z_i)^2$. Here, we use $\alpha = HOMO$ for all the occupied states and $\alpha = LUMO$ for all the unoccupied states.

At this point, it is worth mentioning that the presented $\Delta_\alpha$ expression is the more remarkable difference with the implementation proposed in Refs.[35, 36]. These authors compute the image-charge correction term using the expression:

$$\Delta_\alpha = \frac{1}{8\pi\varepsilon_0}\sum_i \frac{|q_i^\alpha|^2}{2(x_i - x_t)} + \frac{|q_i^\alpha|^2}{2(x_i - x_b)}, \tag{10}$$

where $x_t$ and $x_b$ represent the location of the top and bottom image planes, respectively. In Appendix B, we discuss the effect of the image charge correction in the computed values.

Taking into account the two contributions, frontier orbitals and image-charge, we can obtain the total correction to the occupied, $\Sigma_{occ}$, and unoccupied states, $\Sigma_{unocc}$, as:

$$\Sigma_{occ} = -\varepsilon_H - IP + \Delta_{HOMO} \tag{11}$$

$$\Sigma_{unocc} = -\varepsilon_L - EA - \Delta_{LUMO} \tag{12}$$

Finally, we obtain a new modified molecular Hamiltonian, $\boldsymbol{H_{mol,\Sigma}}$, which replaces the sub-matrix $\boldsymbol{H_{mol}}$ in the SR Hamiltonian,

$$\boldsymbol{H_{mol,\Sigma}} = \boldsymbol{H_{mol}} + \boldsymbol{\Sigma} \tag{13}$$

### *2.3. Implementation for TranSIESTA*

To correct and replace the molecular Hamiltonian, first, we have to extract the SR Hamiltonian, $\boldsymbol{H_{KS,k}}$, from the '.TSHS' file obtained from the TranSIESTA calculation. Then, from $\boldsymbol{H_{KS,k}}$, we extract the molecular Hamiltonian, $\boldsymbol{H_{mol}}$, and the overlap matrix, $\boldsymbol{S_{mol}}$. To this end, we have employed the Python libraries sisl [45] and NumPy[46] in combination with the Atomic Simulation Environment (ASE)[47, 48]. In order to obtain the eigenvalues $\varepsilon_\alpha$ and eigenvectors $\boldsymbol{\psi_\alpha}$, we diagonalize $\boldsymbol{H_{mol}}$,

$$\boldsymbol{H_{mol}}\boldsymbol{\psi^\alpha} = \varepsilon_\alpha \boldsymbol{S_{mol}}\boldsymbol{\psi^\alpha}. \tag{14}$$

Here $\boldsymbol{\psi_\alpha}$ is expanded in a non-orthonormal basis set $\{\boldsymbol{\theta_{i,\nu}}\}$, for the atom $i$ and atomic orbital $\nu$,

$$\boldsymbol{\psi^\alpha} = \sum_i \sum_\nu c_{i,\nu}^\alpha \boldsymbol{\theta_{i,\nu}}. \tag{15}$$

To obtain the point charge distribution (see eq.7), we have to define the eigenvectors in an orthonormal basis set. To this end, we first diagonalize $\boldsymbol{S_{mol}}$, $\boldsymbol{S_{mol}}\boldsymbol{d^\alpha} = k_\alpha \boldsymbol{d^\alpha}$, obtaining the diagonalized overlap matrix $\boldsymbol{\tilde{S}_{mol}}$, such as:

$$\boldsymbol{D}^{-1}\boldsymbol{S_{mol}}\boldsymbol{D} = \boldsymbol{\tilde{S}_{mol}}, \tag{16}$$

where $\boldsymbol{D}$ is an eigenvector matrix with $\boldsymbol{d^\alpha}$ column vectors. Then, we define a new real, symmetric, and hermitian matrix $\boldsymbol{A}$ with column vectors $\boldsymbol{a^\alpha} = \frac{1}{\sqrt{k_\alpha}}\boldsymbol{d^\alpha}$, so that, $\boldsymbol{A^\dagger S_{mol} A} = \boldsymbol{I}$. We define a new vector $\boldsymbol{\varphi^\alpha} = \boldsymbol{A^{-1}}\boldsymbol{\psi^\alpha}$, which can replace $\boldsymbol{\psi^\alpha}$ in eq. 14, such as:

$$\boldsymbol{A}^{\dagger}\boldsymbol{H_{mol}}\boldsymbol{A}\boldsymbol{\varphi}^{\boldsymbol{\alpha}} = \varepsilon_{\alpha}\boldsymbol{A}^{\dagger}\boldsymbol{S_{mol}}\boldsymbol{A}\boldsymbol{\varphi}^{\boldsymbol{\alpha}} = \varepsilon_{\alpha}\boldsymbol{\varphi}^{\boldsymbol{\alpha}}. \tag{17}$$

From this equation, we can see that $\boldsymbol{\varphi}^{\boldsymbol{\alpha}}$ is an eigenvector of the operator $\boldsymbol{A}^{\dagger}\boldsymbol{H_{mol}}\boldsymbol{A}$ with the same eigenvalues as $\boldsymbol{H_{mol}}$. However, its eigenvectors are expanded in an orthonormal basis set $\{\boldsymbol{\phi_{i,\nu}}\}$.

Going back to eqs. 7-13 , we obtain a diagonal matrix $\tilde{\boldsymbol{\Sigma}}$, where $\tilde{\Sigma}_{ij} = 0$ if $i \neq j$, with:

$$\tilde{\Sigma}_{ii} = \begin{cases} \Sigma_{occ} & ; \text{if } i \in \text{occ} \\ \Sigma_{unocc} & ; \text{if } i \in \text{unocc} \end{cases} \tag{18}$$

Now, to solve equation 13, we have to rotate the $\tilde{\boldsymbol{\Sigma}}$ matrix to the initial non-orthogonal basis set. To do so, we have to go back to equation 17, which allows us to write:

$$\boldsymbol{\varphi}^{-1}\boldsymbol{A}^{\dagger}\boldsymbol{H_{mol}}\boldsymbol{A}\boldsymbol{\varphi} = \boldsymbol{E}, \tag{19}$$

where $\boldsymbol{\varphi} = \boldsymbol{A^{-1}}\boldsymbol{\psi}$ is the eigenvector matrix with column $\boldsymbol{\varphi}^{\boldsymbol{\alpha}}$ and $\boldsymbol{E}$ is the diagonalized Hamiltonian. Thus,

$$\boldsymbol{H_{mol}} = \boldsymbol{A}^{\dagger^{-1}}\boldsymbol{\varphi}\boldsymbol{E}(\boldsymbol{A}\boldsymbol{\varphi})^{-1} = (\boldsymbol{A}\boldsymbol{A}^{\dagger})^{-1}\boldsymbol{\psi}\boldsymbol{E}\boldsymbol{\psi}^{-1}. \tag{20}$$

Analogously,

$$\boldsymbol{\Sigma} = (\boldsymbol{A}\boldsymbol{A}^{\dagger})^{-1}\boldsymbol{\psi}\tilde{\boldsymbol{\Sigma}}\boldsymbol{\psi}^{-1}, \tag{21}$$

where $\boldsymbol{\psi}$ is a matrix with $\boldsymbol{\psi}^{\boldsymbol{\alpha}}$ columns. Once $\boldsymbol{H_{mol,\Sigma}}$ is constructed we write a new '.TSHS' file to compute the transmission with the TBTRANS extension [13].

### *2.4. Specific calculation parameters*

In this section, we discuss the specific parameters that have been used in the benchmark calculations shown in section 3.

*2.4.1. Construction of junction geometries.* The geometry optimizations have been performed within the density functional theory (DFT) generalized gradient approximation GGA (by means of the PBE functional [42]) as implemented in the plane-wave based VASP code[49]. In all cases, projector augmented waves (PAW)[50] were used to describe the interaction of the core electrons with the nuclei, and a cut-off energy of 450 eV has been set for the plane-wave basis. For molecules from 1 to 4 rings (see Fig. 1), we used a 6x6 Au(111) periodic unit cell, and 5 gold layers below and above the molecule, as shown in Fig. 2 red dashed box. To avoid spurious interactions between the slabs, a vacuum layer of 20 Å have been placed between them in the transport direction. A 3×3×1 k-points has been used to sample the first Brillouin zone. For molecules with 5 rings, we have used a 7x7 Au(111) periodic unit cell and only

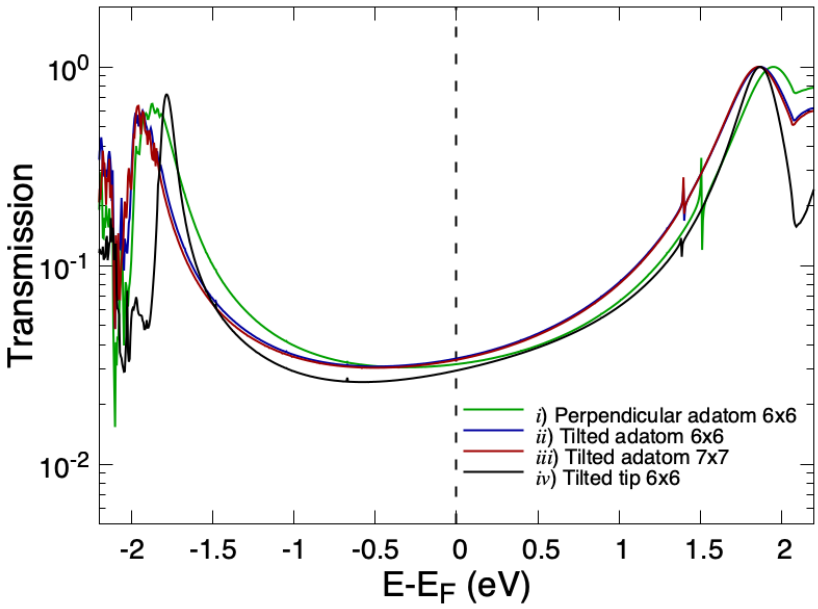


Figure 4: Transmission functions obtained for the B-$(NH_2)_2$ molecule considering several different configurations. *i*) Perpendicular molecule on a 6×6 unit cell surface with adatom; *ii*) tilted molecule on a 6×6 unit cell with adatom; *iii*) same than *ii* but on a 7×7 uni cell surface with adatom; *iv*) tilted molecule on a 6×6 unit cell surface with tip.

the Γ-point to sample the Brillouin zone. In all the junctions studied, the molecule and the two outermost Au layers were relaxed until all the forces were lower than 0.01 eVÅ$^{-1}$. From these optimizations, we have obtained a Au-Au lattice parameter of 2.94 Å and junctions distances, Au-N and Au-S ≈ 2.4 Å. Two orientations for the B-$(NH_2)_2$ molecule, perpendicular and tilted, and two surface junctions (adatom and tip) have been built and tested (see Fig 2).

*2.4.2. Transport properties at DFT-NEGF level.* Transport properties have been obtained by means of the TranSIESTA package, using identical left and right electrodes with three additional Au layers each. To carry out these simulations, we have used the PBE [42] exchange-correlation functional, a double-ζ basis set for all the atoms, and a mesh cutoff energy of 250 Ry (≈ 3401 eV). The first Brillouin zone has been described using a 4×4×1 k-mesh (3×3×1 k-mesh for the 7×7 Au(111) slab). Relativistic effects associated with the Au atoms have been taken into account using norm-conserving pseudopotentials [51]. Using these parameters, and following the method described in Ref [52], we have computed a work function value equal to 4.8 eV, close to the experimental value of 5.2 eV. Once a converged Hamiltonian is obtained, the transmissions are calculated with the TBTRANS code using a 8x8 k-mesh.

To evaluate the dependence of the transmission function on the model used to represent the junction, we have computed and compared both the transmission function

Table 1: DFT Conductances (G) of *i*-*iv* models (see text).

| Configuration | *i* | *ii* | *iii* | *iv* |
|---|---|---|---|---|
| G ($10^{-3}$ $G_0$) | 31.88 | 34.06 | 33.52 | 29.62 |

(see Fig. 4) and the conductance (see Tab. 1) for four junction models, taking the B-$(NH_2)_2$ molecule as benchmark system. The models considered are: (i) the molecule is placed perpendicular to the electrodes, which are represented by a 6×6 unit cell surface with an adatom as molecule-metal contact; (ii) the molecule is tilted and the electrodes are also represented by a 6×6 unit cell surface with an adatom as molecule-metal contact; (iii) same model as in (ii) but with a 7×7 unit cell surface; (iv) the molecule is titled and the electrodes are represented by 6×6 unit cell surface with trigonal pyramidal tip formed by four gold atoms. From the comparison between transmissions and conductances obtained with models (i) and (ii), we can see that the orientation of the molecules does not play a crucial role on the obtained values. Transmissions for model (ii) and (iii) overlap and the conductances are very close to each other. In view of these results we have used a 6x6 unit cell for all systems investigated in this work, B-$(X)_2$, N-$(X)_2$, A-$(X)_2$, and T-$(X)_2$ (see Fig. 1). From the comparison between models (ii) and (iv), we can see a slight decrease of the HOMO-LUMO gap and the conductance. In view of these comparisons, we have chosen the model (iv) as the more realistic one to carry out our simulations.

*2.4.3. Transport properties at DFT+$\mathbf{\Sigma}$ level.* Our methodology is based in the modification of the scattering Hamiltonian as we have described in Sec. 2.3. After obtaining the new Hamiltonian, we employ the TBTRANS code using the same parameters as in the DFT-NEGF calculations. In Tab. 2, we report the correction energies to be used in equation 18 for the occupied and unoccupied orbitals.

## 3. Results and discussion

In the following subsections, we analyze the results of conductances obtained as a function of the molecule size, the type of anchoring group, and its position. As shown in Fig. 1, we have considered acenes up to five fused benzene rings, and, for each molecule, we have considered all possible positions of the anchoring groups with the restriction that they are always attached to the same phenyl ring. Finally, we have studied two possible anchoring groups, amine (-$NH_2$) and methylthio (-SMe).

### *3.1. Diamino-acenes*

The transmission functions for the nine acene molecules considered in this work with $NH_2$ anchoring groups, with (DFT+Σ) and without (DFT) self-energy correction, are displayed in Fig. 5. From this Fig., we can see that transmission functions computed at

Table 2: $-\varepsilon_H - IP$ and $-\varepsilon_L - EA$ are the energy shift from the HOMO and LUMO gas phase level. $\Delta_{HOMO}$ and $-\Delta_{LUMO}$ are the image charge correction of the HOMO and LUMO charge distribution in the junction obtained from eq. 9 (values obtained using eq. 10 are displayed in Tab. 4 of Appendix A). $\Sigma_{occ}$ and $\Sigma_{unocc}$ are the total energy shift to the occupied and unoccupied orbitals of the molecule in the scattering region (see Eq. 11 and 12). All the energies are in eV.

| X=$NH_2$ (SMe) | $-\varepsilon_H - IP$ | $-\varepsilon_L - EA$ | $\Delta_{HOMO}$ | $-\Delta_{LUMO}$ | $\Sigma_{occ}$ | $\Sigma_{unocc}$ |
|---|---|---|---|---|---|---|
| B-$(X)_2$ | -2.73 (-2.33) | 2.78 (2.38) | 0.67 (0.65) | -0.67 (-0.65) | -2.07 (-1.68) | 2.11 (1.74) |
| N-$(X)_2$ | -2.43 (-2.15) | 2.36 (2.18) | 0.68 (0.65) | -0.67 (-0.64) | -1.75 (-1.50) | 1.69 (1.53) |
| $A_1$-$(X)_2$ | -2.18 (-1.93) | 2.11 (1.98) | 0.68 (0.64) | -0.67 (-0.65) | -1.50 (-1.28) | 1.44 (1.33) |
| $A_2$-$(X)_2$ | -2.18 (-1.96) | 2.06 (1.98) | 0.68 (0.64) | -0.68 (-0.64) | -1.50 (-1.32) | 1.39 (1.34) |
| $T_1$-$(X)_2$ | -1.95 (-1.76) | 1.91 (1.81) | 0.68 (0.63) | -0.67 (-0.64) | -1.28 (-1.13) | 1.24 (1.17) |
| $T_2$-$(X)_2$ | -1.98 (-1.80) | 1.88 (1.82) | 0.67 (0.61) | -0.67 (-0.64) | -1.31 (-1.19) | 1.21 (1.18) |
| $P_1$-$(X)_2$ | -1.76 (-1.65) | 1.75 (1.68) | 0.68 (0.65) | -0.67 (-0.65) | -1.09 (-1.00) | 1.09 (1.03) |
| $P_2$-$(X)_2$ | -1.81 (-1.67) | 1.74 (1.68) | 0.67 (0.65) | -0.68 (-0.65) | -1.14 (-1.02) | 1.06 (1.04) |
| $P_3$-$(X)_2$ | -1.82 (-1.67) | 1.72 (1.68) | 0.68 (0.64) | -0.67 (-0.64) | -1.14 (-1.03) | 1.05 (1.04) |

DFT level without correction is quite size-sensitive. Indeed, the transmission function shapes change substantially as a function of both the number of fused rings conforming the acene and the position of the anchoring groups. Transmission functions obtained at DFT+$\Sigma$ level show smaller values and change more smoothly with the number of fused rings and the anchoring group position. From these calculations, we can see that the position of the HOMO remains more or less constant whereas that of the LUMO approaches the Fermi level as the number of fused ring increases, reducing the band gap. On the other hand, Fig. 5 shows that the HOMO-LUMO gap does not depend on the position of the anchoring groups. Finally, a comparison between the transmissions displayed in Fig. 5 and the results presented in Tab. 2 allows us to conclude that, since the image charge effect is almost constant for the molecules studied here, the image charge correction just shifts down the absolute transmission values, whereas the xc-correction in gas phase, that decreases as the number of fused ring increases, is the dominant effect responsible for the behavior of the self-energy correction term as a function of the number of fused rings.

The conductances, which at low temperature can be computed as the value of transmission function at the Fermi level multiplied by the quantum conductance ($G_0$=$2e^2/h$) [31], are displayed in Fig. 6. From this Fig., we observe, on the one hand, that conductances decrease by more than an order of magnitude when the DFT+$\Sigma$ approach is applied. On the other hand, we observe that the behavior of the conductance as a function of the number of fused rings and the anchoring-group positions does follow the same trend disregarding the type of calculation DFT or DFT+$\Sigma$. The conductance increases monotonously from bencene-$(NH_2)_2$ to pentacene-$(NH_2)_2$ for the same position of the anchoring groups (the edge or center ring). Focusing on the conductance of the anthracene-$(NH_2)_2$, tetrachene-$(NH_2)_2$ and pentacene-$(NH_2)_2$, we observe a sharp

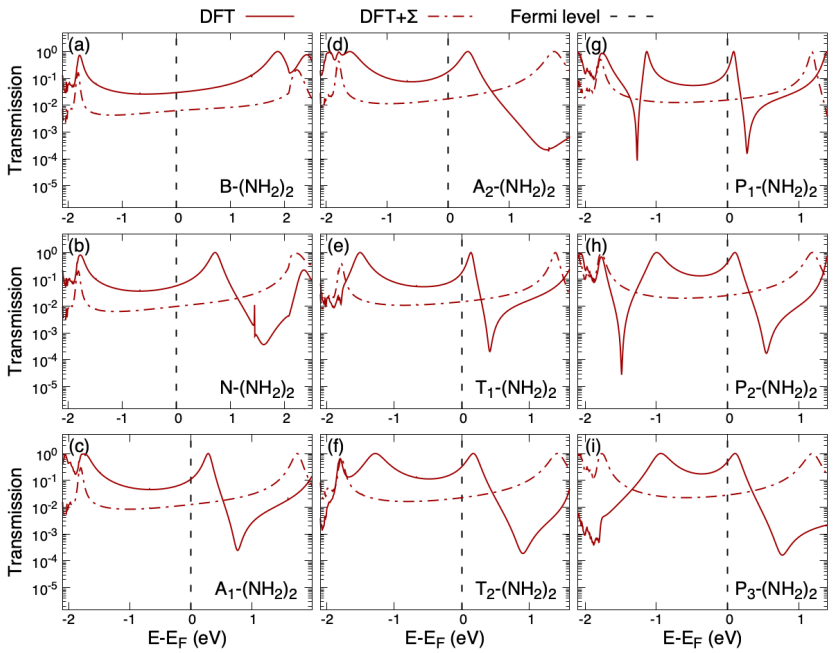


Figure 5: Transmission function calculated with DFT (solid red line) and DFT+Σ (dashed red line). The vertical dashed black line points the Fermi level. The structures of molecules are shown in Fig. 1.

enhancement when the anchoring groups move from the edge to the center ring, so that the conductance of $A_2$-$(NH_2)_2$ (see Fig. 1) is higher than that of $T_1$-$(NH_2)_2$ and $P_1$-$(NH_2)_2$, and the conductance of $T_2$-$(NH_2)_2$ is higher than that of $P_1$-$(NH_2)_2$. At this point, it also worth mentioning that, as shown in Fig. 4 of Ref. [53], Ac-$(NH_2)_2$ conductances follow the same trend as the $HOMO_{Huckel}$ levels, where Ac stands for acene molecules, which allows us to conclude that the transmissions, and therefore the conductances, are non-resonantly HOMO dominated.

### *3.2. Bismethylthio-acenes*

Transmission functions for Ac-$(SMe)_2$ are shown in Fig. 7. From the comparison between this Fig. and Fig. 5, we can conclude that, whereas the transmission function computed with DFT at the Fermi level barely depends on the nature of the anchoring group, it does show a measurable dependence when the Σ correction is applied. This effect reflects in the calculated conductances. Conductances for Ac-$(SMe)_2$ complexes are displayed in Fig. 6 together with those of Ac-$(NH_2)_2$. From this Fig., we can see that G values computed at DFT theory level for both groups of complexes, Ac-$(SMe)_2$ and Ac-$(NH_2)_2$, show the same trend as a function of the number of benzene rings and anchoring-group position. Furthermore, absolute values of G are very similar, only lightly higher, in general, for Ac-$(SMe)_2$ complexes, except for $P_2$ and $P_3$ molecules for which $P_2$-$(NH_2)_2$ and $P_3$-$(NH_2)_2$ complexes show slightly higher G values than $P_2$-$(SMe)_2$ and $P_3$-$(SMe)_2$ complexes. The scenario is completely different upon application

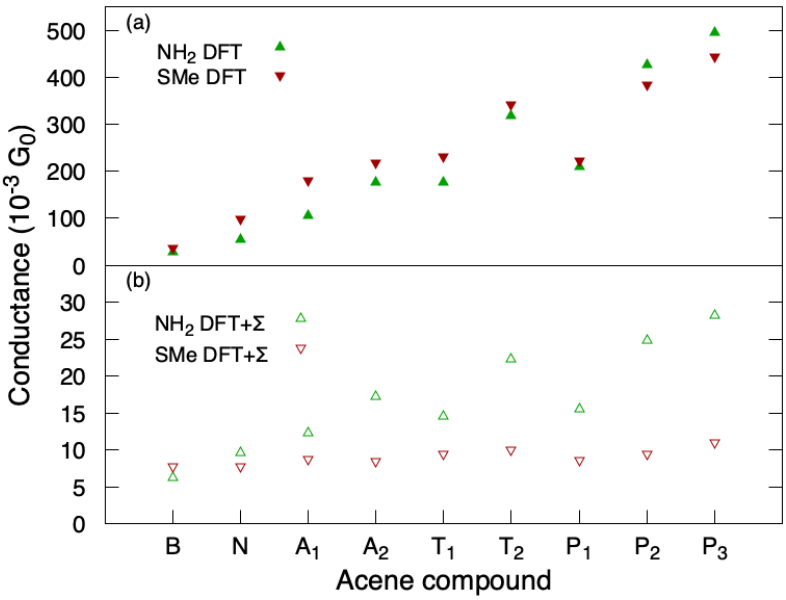


Figure 6: Conductances for the nine molecules studied here (see Fig. 1) before (a) and after (b) self-energy correction.

of the Σ correction. From Fig. 6 (b), we observe that the conductance for Ac-$(SMe)_2$ is almost constant across the complexes studied, contrary to the behavior observed for Ac-$(NH_2)_2$ complexes as discuss above. As widely discussed in Ref. [53], the difference in conductance behavior observed between Ac-$(NH_2)_2$ and Ac-$(SMe)_2$ complexes, at the DFT+Σ theory level, is mainly due to the nature of the coupling between the lone pairs located in the anchoring groups and the $\pi$ and $d$ orbitals of the molecules and the electrodes, respectively. In the Ac-$(NH_2)_2$ complexes, the anchoring groups does not modify appreciably the electron distribution in the acene rings with respect to the corresponding pristine acene, and the lone pair located in the nitrogen atoms couples more strongly with the $\pi$ orbitals of the acene molecules than with the $d$ orbitals of the gold electrodes -because the lone pair is nearly perpendicular to the plane of the molecule. This strong coupling between the N lone pair and the acenes $\pi$ orbitals favors the electron transport through the disubstituted ring. Thus, the higher the conjugation of the lone pair of the anchoring group with the acene $\pi$-orbital the higher the conductance. On the other hand, for Ac-$(SMe)_2$ complexes, the electron transport through the disubstituted ring is hindered due to: (i) the high electron affinity of sulfur atoms that favor the locatization of electrons on their vicinity; (ii) the weak coupling between the two lone pairs located on the sulfur atoms and the $\pi$ orbitals of the molecules. As a consequence, the conductance does not depend significantly on the number of fused rings present in the acene.

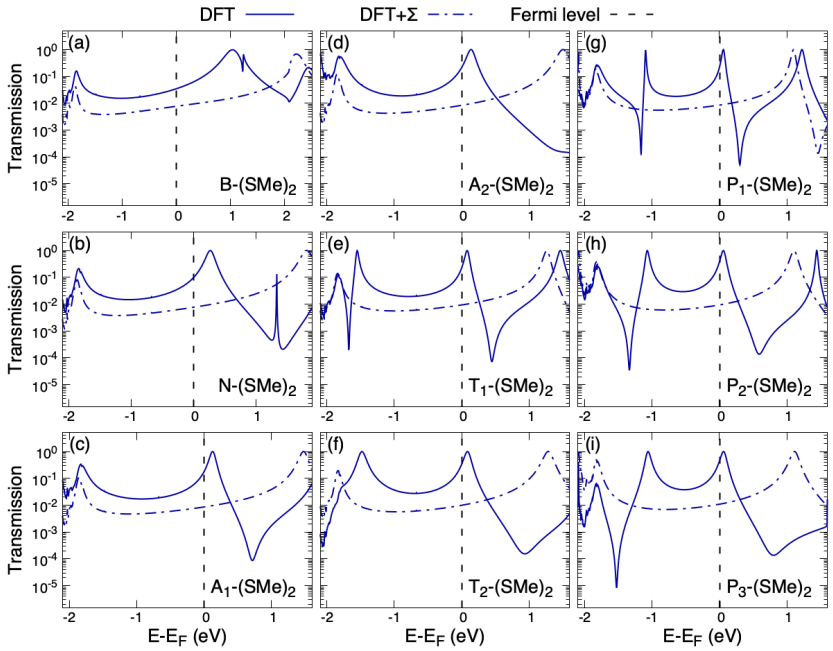


Figure 7: Transmission function calculated with DFT (solid blue line) and DFT+Σ (dashed blue line). The vertical dashed black line is the Fermi level.

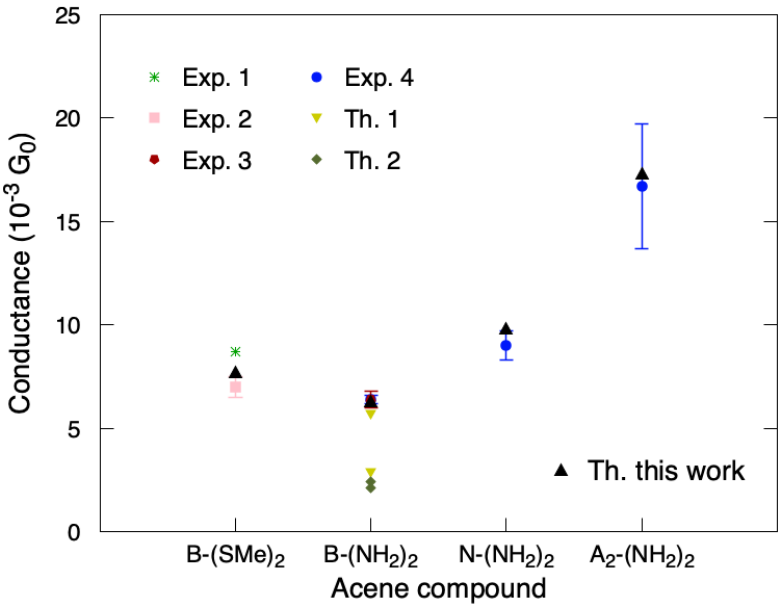


Figure 8: Conductance for several Ac-$(X)_2$ molecules. Black triangles represent our results. Experimental measurements are represented as green asterisk (Exp.1) [54], pink square (Exp.2) [55], red pentagon (Exp.3) [56] and blue circles (Exp.4) [57]. Previous theoretical results are represented as yellow triangles (Th.1) [17] and dark green rhombus (Th.2) [31].

### *3.3. Comparison with previous theoretical and experimental results*

Finally, we have tested the accuracy of our implementation of self-energy corrected DFT-NEGF in TranSIESTA package by comparing the conductance obtained for the complexes B-$(SMe)_2$, B-$(NH_2)_2$, N-$(NH_2)_2$, and $A_2$-$(NH_2)_2$ with previous theoretical and/or experimental data available in the literature. From Fig. 8, where we compare our results with previous ones, we can see that our simulations reproduce quantitatively experimental measurements, within experimental error bars. Furthermore, our simulation for the B-$(NH_2)_2$ complex reproduces the experimental measurement more accurately than previous theoretical simulations[31, 17], also based on DFT+Σ. In addition, the use of equation 9 and 10 to compute the image charge effect, leads to conductance values closer to the experimental ones in the former case (see Table S1 in the SI). all of it, shows the importance of achieving a correct description of the image-charge effect.

In this respect Markussen et al. [17] already showed that calculated conductances are only close to the experimental values when the image plane is located 1 Å outside the tip, for the image plane located 1 Å inside the tip the simulated conductance moved away from the experimental. In our simulation the image plane is located 1.47 Å outside the surface layer average (neglecting the adatom/tip). A detailed analysis of the dependence of the conductance values with the location of the image plane can be found in Appendix B (Tab. 5 and Fig. 9). At this point, it is worth noticing that the optimal image plane location will depend on the specific metal electrodes employed

Finally, it is worth mentioning that the DFT+Σ implementation presented here has also been shown to yield conductance values in very good agreement with experimental measurements for similar molecules, such as PhSMe-benzene-PhSMe [58], PhSMe-anthracene-PhSMe [58] (PhSMe=(4-methylthio)phenyl), and in good agreement for more complex molecules, such as diamino-1,4-azaborine-anthracene [59], diamino-1,4-azaborine-pentacene [59], and 6,12-Bis-(2,6,-dimethyl-4-methylthio-phenulthynyl)indieno[1,2-b]Z [60]. Conductance values computed for all these molecular junctions, and the corresponding experimental measurements, are given in Tab. 3

## 4. Conclusions

In summary, we have presented a robust implementation of the DFT+Σ approach, which allows one to correct the alignment of the molecular levels yielded by standard DFT, in the framework to the TranSIESTA package. Using as benchmark systems a family of acene molecules, from benzene to pentacene, and amino (-$NH_2$) and methyl sulfide (SMe) as anchoring groups, we have assessed our implementation by a direct comparison of our simulated conductances with previous experimental and/or theoretical results. The good agreement obtained proves the accuracy of our implementation.

From the comparison between transmission functions and conductances obtained for Ac-$(NH_2)_2$ and Ac-$(SMe)_2$ complexes at DFT and DFT+Σ energy level, we have

| Molecule | $\log(G/G_0)_{DFT+\Sigma}$ | $\log(G/G_0)_{Exp.}$ |
|---|---|---|
| 1,4 bis(methylthio)benzene | -2.11[a] | -2.06[b]<br>-2.15 ± 0.06[c] |
| 1,4 diamine-benzene | -2.20[a]<br>-2.54 - -2.24[f]<br>-2.68 - -2.62[g] | -2.19 ± 0.08[d]<br>-2.19 ± 0.03[e] |
| 1,4 diamino-naphthalene | -2.01[a] | -2.05 ± 0.07[g] |
| 9,10 diamine-Anthracene | -1.76[a] | -1.77 ± 0.16[g] |
| 1,4 bis(4-methylthio)phenyl)-benzene$_2$ | -3.4[h] | -3.7 ± 0.7[i] |
| 1,4 bis(4-methylthio)phenyl)-anthracene$_2$ | -5.0[h] | -5.2 ± 0.31[j] |
| diamino-1,4-azaborine-anthracene | -6.30[i] | -5.60 ± 0.33[i] |
| diamino-1,4-azaborine-pentacene | -6.45[i] | -5.90 ± 0.40[i] |
| 6,12-Bis-(2,6-dimethyl-4-methylthio-phenylthynyl)indieno[1,2-b] | -3.27[k] | -3.60[k] |

Table 3: Calculated DFT+Σ zero bias and experimentally measured conductance values ($\log(G/G_0)$) in the single molecule-junctions. [a] This work; [b] data from Ref. [54]; [c] data taken from [55]; [d] data from Ref. [56]; [e] data from Ref. [57]; [f] data from Ref. [17]; [g] data from Ref. [31]; [h] data from Ref. [58]; [i] data from Ref. [59]; [j] data from Ref. [61]; [k] data from Ref. [60].

assessed: (i) the importance of correcting the DFT HOMO-LUMO energy gap and of correctly including the effect of the image charges; (ii) the influence of the anchoring group on the conductance, so that the stronger (weaker) the binding energy between the anchoring group and the molecule (the metal electrode) the higher the conductance.

## Acknowledgments

We acknowledge the allocation of computer time by the Red Española de Supercomputación (RES) and the Centro de Computación Científica at the Universidad Autónoma de Madrid (CCC-UAM). This work has been supported by the MICINN projects PID2019-105458RB-I00 and PID2019-106732GB-I00, 'Severo Ochoa' Programme for Center of Excellence in R&D (SEV-2016-0686), 'María de Maeztu'

Programme for Units of Excellence in R&D (CEX2018-000805-M).

## Appendix A

In Tab. 4, we compare the image charge corrections ($\Delta_{HOMO/LUMO}$) computed using Eq. 9 and those obtained from Eq. 10 used in Refs. [35, 36]. To perform this comparison, we have select three representative molecules, anthracene-diamine ($A_2$-$(NH_2)_2$), tetracene-diamine ($T_1$-$(NH_2)_2$)), and pentacene-diamine ($P_1$-$(NH_2)_2$)). From the values displayed in this Tab., one can see that Eq. 9 yields correction values between 15% and 20% smaller than those obtained from Eq. 10. Thus, by applying Eq. 9 to include image charge effects, one obtains conductance values between 12% and 16% smaller than by applying Eq. 10.

Table 4: Comparison of the correction energies ($\Sigma_{occ/unocc}$) in the DFT+$\Sigma$ method and their corresponding zero-bias conductances (G) using equation 9 and 10 to compute the image charge effects ($\Delta_{HOMO/LUMO}$).

| Molecule | Equation | $\Delta_{HOMO}$ | -$\Delta_{LUMO}$ | $\Sigma_{occ}$ | $\Sigma_{unocc}$ | G($10^{-3}$ $G_0$) |
|---|---|---|---|---|---|---|
| $A_2$-$(NH_2)_2$ | 9 | 0.68 | -0.68 | -1.50 | 1.39 | 17.33 |
| | 10 | 0.84 | -0.80 | -1.34 | 1.26 | 19.82 |
| $T_1$-$(NH_2)_2$ | 9 | 0.68 | -0.67 | -1.28 | 1.24 | 14.64 |
| | 10 | 0.85 | -0.82 | -1.10 | 1.09 | 17.10 |
| $P_1$-$(NH_2)_2$ | 9 | 0.68 | -0.67 | -1.09 | 1.09 | 15.61 |
| | 10 | 0.86 | -0.82 | -0.90 | 0.93 | 18.65 |

## Appendix B

In Tab. 5, we show, for the benchmark molecule Bencene-diamine (B-$(NH_2)_2$), data for image charge effects ($\Delta_{HOMO/LUMO}$), corrections energies ($\Sigma_{occ/unocc}$), and conductance values (G) obtained as a function of the image plane distance (d) -measured with respect to the outermost gold flat layer. From this Tab., one can observe an increase of the conductive values when d increases. From Fig. 9, one can see that the dependence of the G with d is linear, given by the equation:

$$G = (5.80 \pm 0.03) + (0.35 \pm 0.02)d, \tag{22}$$

with a coefficient of determination, $R^2$, equal of 0.9899 and a Pearson correlation coefficient equal la to 0.9950. From this Fig., we can also see that any d values between 1.14 and 2.28 Å leads to a conductance value within the experimental range, 6.2 $10^{-3}G_0$-6.6 $10^{-3}G_0$. (see Refs. [54, 55]). As explained in the main text, we have used d=1.47 Å [62, 43, 31]. Strictly speaking, this value is only valid for a perfectly flat gold surface, because the screening introduced by the tip may modified slightly the image plane

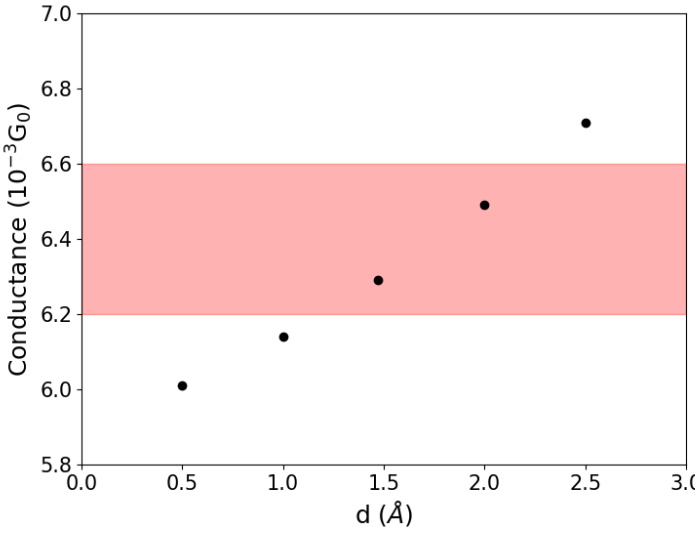


Figure 9: Conduntance values for the $B(NH_2)_2$ molecules (see Fig. 1) as a function of the image plane distances (d). d=0 is taken as the outermost gold flat layer (see Fig. 3). The shadow region represent the experimental range values [54, 55].

distance. However, as shown in Fig. 9 a slight variation of d will barely affect the good agreement between theory and experiment.

Table 5: Conductance values for the B-$(NH_2)_2$ molecule (see Fig. 1) as a function of the image plane distances (d).

| d(Å) | $\Delta_{HOMO}$ | -$\Delta_{LUMO}$ | $\Sigma_{occ}$ | $\Sigma_{unocc}$ | G($10^3$ $G_0$) |
|---|---|---|---|---|---|
| 0.50 | 0.59 | -0.59 | -2.14 | 2.19 | 6.01 |
| 1.00 | 0.63 | -0.63 | -2.11 | 2.15 | 6.14 |
| 1.47 | 0.67 | -0.67 | -2.07 | 2.11 | 6.29 |
| 2.00 | 0.72 | -0.72 | -2.01 | 2.06 | 6.49 |
| 2.50 | 0.78 | -0.78 | -1,96 | 1.99 | 6.71 |

## Conflicts of interest

The authors declare no conflict of interest.

## References

[1] Aviram A and Ratner M A 1974 *Chem. Phys. Lett.* **29** 277
[2] McCreery R L 2004 *Chem. Mater* **16** 4477
[3] McCreery R L and Bergren A J 2009 *Adv. Mater.* **21** 4303
[4] Solomon G C, Herrmann C and Ratner M A 2012 Unimolecular and supramolecular electronics ii: Chemistry and physics meet at metal-molecule interfaces *Book Series: Topics in Current Chemistry-Series* vol 333 (2012)

[5] Gehring P, Thijssen J M and van der Zant H S 2019 *Nature Rev. Phys.* **1** 381
[6] Kim Y and Song H 2021 *Phys. Rev.* **8** 011303
[7] Slowinski K and Majda M 2000 *J. Elecroanal. Chem* **491** 139
[8] Cui X D, Primak Z, Zarate X, Tomfohr J, Sankey O F, Moore A L, Moore T A, D G, Harris G and Lindsay S M 2001 *Science* **294** 571
[9] Kushmerick J G, Holt D B, Yang J C, Naciri J, Moore M H and Shashidhar R 2002 *Phys. Rev. Lett.* **89** 086802
[10] Garcia-Lastra J M, Rostgaard C, Rubio A and Thygesen K S 2009 *Phys. Rev. B* **80** 245427
[11] Kurth S and Stefanucci G 2013 *Phys. Rev. Lett.* **111** 030601
[12] Stefanucci G and Kurth S 2015 *Nano Letters* **15** 8020
[13] Papior N, Lorente N, Frederiksen T, García A and Brandbyge M 2017 *Computer Physics Communications* **212** 8
[14] Landauer R 1957 *IBM Journal of Research and Development* **1** 223
[15] Darancet P, Widawsky J R, Choi H J, Venkataraman L and Neaton J B 2012 *Nano Letters* **12** 6250
[16] Jin C, Strange M, Markussen T, Solomon G C and Thygesen K S 2013 *The Journal of Chemical Physics* **139** 184307
[17] Markussen T, Jin C and Thygesen K S 2013 *physica status solidi (b)* **250** 2394
[18] Khoo K H, Chen Y, Li S and Quek S Y 2015 *Phys. Chem. Chem. Phys.* **17** 77
[19] Inkpen M S, Liu Z F, Li H, Campos L M, Neaton J B and Venkataraman L 2019 *Nature Chemistry* **11** 351
[20] Sau J D, Neaton J B, Choi H J, Louie S G and Cohen M L 2008 *Phys. Rev. Lett.* **101** 026804
[21] Thygesen K S 2008 *Phys. Rev. Lett.* **100** 166804
[22] Strange M and Thygesen K S 2012 *Phys. Rev. B* **86** 195121
[23] Baer R and Neuhauser D 2005 *Phys. Rev. Lett.* **94** 043002
[24] Livshits E and Baer R 2007 *Phys. Chem. Chem. Phys.* **9** 2932–2941
[25] Liu Z F, Egger D A, Refaely-Abramson S, Kronik L and Neaton J B 2017 *The Journal of Chemical Physics* **146** 092326
[26] Yamada A, Feng Q, Hoskins A, Fenk K D and Dunietz B D 2016 *Nano Letters* **16** 6092–6098
[27] Quek S Y, Venkataraman L, Choi H J, Louie S G, Hybertsen M S and Neaton J B 2007 *Nano Letters* **7** 3477
[28] Mowbray D J, Jones G and Thygesen K S 2008 *The Journal of Chemical Physics* **128** 111103
[29] Quek S Y, Choi H J, Louie S G and Neaton J B 2009 *Nano Letters* **9** 3949
[30] Quek S Y, Choi H J, Louie S G and Neaton J B 2011 *ACS Nano* **5** 551
[31] Zotti L A, Bürkle M, Pauly F, Lee W, Kim K, Jeong W, Asai Y, Reddy P and Cuevas J C 2014 *New Journal of Physics* **16** 015004
[32] Choi H J, Cohen M L and Louie S G 2007 *Phys. Rev. B* **76** 155420
[33] Enkovaara J, Rostgaard C, Mortensen J J, Chen J, Dułak M, Ferrighi L, Gavnholt J, Glinsvad C, Haikola V, Hansen H A, Kristoffersen H H, Kuisma M, Larsen A H, Lehtovaara L, Ljungberg M, Lopez-Acevedo O, Moses P G, Ojanen J, Olsen T, Petzold V, Romero N A, Stausholm-Møller J, Strange M, Tritsaris G A, Vanin M, Walter M, Hammer B, Häkkinen H, Madsen G K H, Nieminen R M, Nørskov J K, Puska M, Rantala T T, Schiøtz J, Thygesen K S and Jacobsen K W 2010 *Journal of Physics: Condensed Matter* **22** 253202
[34] Furche F, Ahlrichs R, Hättig C, Klopper W, Sierka M and Weigend F 2014 *WIREs Computational Molecular Science* **4** 91–100
[35] Montes E and Vázquez H 2021 *Appl. Sci* **11** 802
[36] Montes E and Vázquez H 2021 *J. Phys. Chem. C* **125** 825825
[37] Thygesen K S and Rubio A 2008 *Phys. Rev. B* **77** 115333
[38] Strange M, Rostgaard C, Häkkinen H and Thygesen K S 2011 *Phys. Rev. B* **83** 115108
[39] Janak J F 1978 *Phys. Rev. B* **18** 7165
[40] Koopmans T 1934 *Physica* **1** 104

[41] Frisch M J, Trucks G W, Schlegel H B, Scuseria G E, Robb M A, Cheeseman J R, Scalmani G, Barone V, Petersson G A, Nakatsuji H, Li X, Caricato M, Marenich A V, Bloino J, Janesko B G, Gomperts R, Mennucci B, Hratchian H P, Ortiz J V, Izmaylov A F, Sonnenberg J L, Williams-Young D, Ding F, Lipparini F, Egidi F, Goings J, Peng B, Petrone A, Henderson T, Ranasinghe D, Zakrzewski V G, Gao J, Rega N, Zheng G, Liang W, Hada M, Ehara M, Toyota K, Fukuda R, Hasegawa J, Ishida M, Nakajima T, Honda Y, Kitao O, Nakai H, Vreven T, Throssell K, Montgomery Jr J A, Peralta J E, Ogliaro F, Bearpark M J, Heyd J J, Brothers E N, Kudin K N, Staroverov V N, Keith T A, Kobayashi R, Normand J, Raghavachari K, Rendell A P, Burant J C, Iyengar S S, Tomasi J, Cossi M, Millam J M, Klene M, Adamo C, Cammi R, Ochterski J W, Martin R L, Morokuma K, Farkas O, Foresman J B and Fox D J 2016 Gaussian 16 Revision C.01 gaussian Inc. Wallingford CT

[42] Perdew J P, Burke K and Ernzerhof M 1996 *Phys. Rev. Lett.* **77** 3865

[43] Widawsky J R, Darancet P, Neaton J B and Venkataraman L 2012 *Nano Letters* **12** 354

[44] Neaton J B, Hybertsen M S and Louie S G 2006 *Phys. Rev. Lett.* **97** 216405

[45] Papior N 2019 sisl: v0.9.7

[46] Harris C R, Millman K J, van der Walt S J, Gommers R, Virtanen P, Cournapeau D, Wieser E, Taylor J, Berg S, Smith N J, Kern R, Picus M, Hoyer S, van Kerkwijk M H, Brett M, Haldane A, del R'ıo J F, Wiebe M, Peterson P, G'erard-Marchant P, Sheppard K, Reddy T, Weckesser W, Abbasi H, Gohlke C and Oliphant T E 2020 *Nature* **585** 357

[47] Bahn S R and Jacobsen K W 2002 *COMPUTING IN SCIENCE & ENGINEERING* **4** 56

[48] Larsen A H, Mortensen J J, Blomqvist J, Castelli I E, Christensen R, Dułak M, Friis J, Groves M N, Hammer B, Hargus C, Hermes E D, Jennings P C, Jensen P B, Kermode J, Kitchin J R, Kolsbjerg E L, Kubal J, Kaasbjerg K, Lysgaard S, Maronsson J B, Maxson T, Olsen T, Pastewka L, Peterson A, Rostgaard C, Schiøtz J, Schütt O, Strange M, Thygesen K S, Vegge T, Vilhelmsen L, Walter M, Zeng Z and Jacobsen K W 2017 *Journal of Physics: Condensed Matter* **29** 273002

[49] Kresse G and Furthmüller J 1996 *Phys. Rev. B* **54** 11169

[50] Kresse G and Joubert D 1999 *Phys. Rev. B* **59** 1758

[51] Fallaque-Najar J, Morales-Gomero J C and Timon V 2019 *Surf. Sci.* **689** 121458

[52] García-Gil S, García A, Lorente N and Ordejón P 2009 *Phys. Rev. B* **79** 075441

[53] Fallaque J G, Rodríguez-González S, Díaz C and Martín F 2022 *Nanoscale* **14**(2) 464–472

[54] Ahn S, Aradhya S V, Klausen R S, Capozzi B, Roy X, Steigerwald M L, Nuckolls C and Venkataraman L 2012 *Phys. Chem. Chem. Phys.* **14** 13841

[55] Park Y S, Widawsky J R, Kamenetska M, Steigerwald M L, Hybertsen M S, Nuckolls C and Venkataraman L 2009 *Journal of the American Chemical Society* **131** 10820

[56] Venkataraman L, Klare J E, Tam I W, Nuckolls C, Hybertsen M S and Steigerwald M L 2006 *Nano Letters* **6** 458

[57] Quinn J R, Foss F W, Venkataraman L, Hybertsen M S and Breslow R 2007 *Journal of the American Chemical Society* **129** 6714

[58] Fallaque J G, Rodríguez-González S, Díaz C and Martín F 2022 *Nanoscale* **14** 464–472

[59] Palomino-Ruiz L, Rodríguez-González S, Fallaque J G, Márquez I R, Agrait N, Díaz C, Leary E, Cuerva J M, Campana A G, Martín F, Millán A and González M T 2021 *Angew. Chem. Int. Ed.* **60** 6609

[60] Casares R, Martínez-Pinel A, Rodríguez-González S, Márquez I I, Lezama L, González M T, Leary E, Blanco V, Fallaque J G, Díaz C, Martín F, Cuerva J M and Millán A *J. Mater. Chem. C* **Accepted**

[61] Sacchetti V, Ramos-Soriano J, Illescas B M, González M T, Li D, Palomino-Ruiz L, Márquez I R, Leary E, Rubio-Bollinger G, Pauly F, Agrait N and Martín N 2019 *J. Phys. Chem. C* **123** 29386–29393

[62] Lam S C and Needs R J 1993 *Journal of Physics: Condensed Matter* **5** 2101